CdS@C nanowires with rich sulfur vacancies for high-performance lithium storage anodes

Wenhua Tian[1] · Peng Bai[1] · Zihan Wang[1] · Guoqiang Ling[2] · Jing Ren[2] · Rui-Peng Ren[1,3] · Yongkang Lv[1,3]

Abstract

Here, we have prepared carbon-coated cadmium sulfide nanowires with sulfur defect (Vs-CdS NWs@C) anode by a polyvinylpyrrolidone (PVP)-assisted solvothermal method. Vs-CdS NWs@C anode not only increases the wettability of the electrode material and the electrolyte but also exposes more active sites, which can effectively alleviate the volume expansion during the charging and discharging process, accelerate the reaction kinetics, and maintain the stability of the electrode structure. At the same time, the surface defects engineered to construct unsaturated active sites on the surface contribute to the conductivity and introduce active sites for binding lithium ions. Finally, the conductivity of the carbon layer can effectively improve the electrode conductivity. Therefore, the synergistic regulation strategy of nanostructures, sulfur defect engineering, and carbon coating is expected to construct new and efficient anode materials for LIBs.

Keywords Lithium-ion batteries · Anode · Nanowires · Sulfur defects · Carbon coatings

Introduction

With the unprecedented human demand for portable electronic products and electric vehicles, lithium-ion batteries with high energy density, high cycling stability, high safety, and long life become particularly important in the whole energy system [1, 2]. Nevertheless, the graphite is hardly to meet the increasing demand for the high performance of LIBs. Therefore, it is urgent to develop high-capacity anode materials for LIBs. Metal sulfides such as iron sulfide [3–6], vanadium sulfide [7–10], nickel sulfide [11–14], and molybdenum disulfide [15–19] have been extensively studied for their excellent electrical conductivity, mechanical stability, and thermodynamic stability. Among metal sulfides, cadmium sulfide (CdS) has been widely used in photocatalysis,

electrochemical sensors, light-emitting diodes, and solar cells due to its desired direct band gap (2.4 eV), excellent transport properties, and high electron mobility [20–26]. Therefore, it is necessary to investigate CdS as an anode material for LIBs due to its abundant resources and low price.

However, the huge volume change resulting in poor cycle life during the change and discharge process was the key issue of CdS anode. Consequently, a great deal of effort has been devoted to addressing the above-mentioned drawbacks of electrodes, and various strategies have been developed. Firstly, the construction of nanostructures has been conducted for the preparation of high-performance anodes for LIBs [27–29]. Wei et al. have prepared MnO nanowire anode with diameters of 5–10 nm via hydrothermal and polymerization-hydrolysis method. This nanowire anode has ultralong cycling stability, with a specific capacity of 757.4 mAh g^{-1} after 1000 cycles at a current density of 1.0 A g^{-1}[30]. Secondly, defect engineering has been applied as a new strategy to improve the performance of electrode materials. The existence of defect engineering is conducive to providing better electronic conductivity, higher ion diffusion mobility, lower interfacial charge transfer resistance, and more electrochemically active sites [31–33]. Liu et al. synthesized a few-layered MoS_2-V_2C-MXene@C with abundant sulfur vacancies via an in situ assembly and carbonization

✉ Jing Ren
  renjing02@tyut.edu.cn

✉ Rui-Peng Ren
  renruipeng@tyut.edu.cn

1 State Key Laboratory of Clean and Efficient Coal Utilization, Taiyuan University of Technology, Taiyuan 030024, China

2 College of Chemistry, Taiyuan University of Technology, Taiyuan 030024, China

3 Shanxi-Zheda Institute of Advanced Materials and Chemical Engineering, Taiyuan 030017, China

strategies. The experimental results showed that this material with high sulfur vacancies provided a capacity of 732.8 mAh g^{-1} after 100 cycles [34]. Finally, the formation of a carbon-coating layer not only facilitates electron transport but also helps to prevent electrode material aggregation during repeated cycling [35, 36]. Yin et al. designed a carbon-coated SnS nanotube composite using polyvinylpyrrolidone and carbon nitride as carbon sources. The carbon-coated SnS anode exhibits an excellent specific capacity of 547.7 mAh g^{-1} after 200 cycles even at a high current density (1.0 A g^{-1}) [37].These strategies benefit from shortening the electron diffusion length, increasing the conductivity, and slowing the volume expansion, resulting in materials with excellent electrochemical performance. Nanowires provide more surface area, which results in the larger electrode–electrolyte contact area and reduced charging/discharging time. And nanowires can accommodate volume expansion, inhibit mechanical degradation, and extend cycle life. In addition, carbon coatings in composites maintains the structural integrity of the electrode materials.

In this study, we have prepared Vs-CdS NWs@C anode by the PVP-assisted solvent-thermal method, which has the following advantages. Firstly, the nanowire structure can not only enlarge the electrode/electrolyte contact and further shortens the diffusion distance of Li$^+$ ions, but also positively alleviate the volume expansion during charging and discharging. Secondly, the surface sulfur defects provide sufficient active sites for sulfur reduction to polysulfides and Li$_2$S nucleation. Thirdly, the close interaction between the nanowire structure and the carbon layer increases the structural stability of the electrode material and improves the electrical conductivity. Owing to these advantages, the Vs-CdS NWs@C anode shows outstanding electrochemical performance.

Experimental section

Synthesis of Vs-CdS NWs@C

In a typical procedure, cadmium acetate dihydrate (0.265 g), thiourea (0.152 g), and polyvinylpyrrolidone (1.6 g) were mixed in deionized water (5 mL) and ethylenediamine (25 mL) solution under stirring for 40 min. Then, the obtained solution was poured into a 50-mL Teflon-lined autoclave and maintained at 100 °C for 20 h. The obtained precipitates were washed several times by deionized water and ethanol after the autoclave cooled to room temperature. Finally, the products were dried by vacuum freeze drying. The dried products was calcined in a tube furnace under a nitrogen atmosphere for 2 h and heated to 800 °C at a rate of 5 °C/min. Pure CdS was prepared for comparison: cadmium acetate dihydrate (0.266 g) and thiourea (0.076 g) were first dissolved in deionized water (30 mL) with continuous

stirring for 20 min. Then, the obtained solution was poured into a 50-mL Teflon-lined autoclave and maintained at 150 °C for 10 h. The obtained precipitates were washed several times by deionized water and ethanol after the autoclave cooled to room temperature. Finally, the products were dried in an oven at 60 °C for 24 h to obtain pure CdS.

Material characterization

The microstructure and morphology were observed by scanning electron microscopy (SEM) at 3 kV (TESCAN MIRA LMS, Czech Republic) and transmission electron microscopy (TEM) at an accelerating voltage of 200 kW (FEI Talos F200X G2, USA). XPS data were collected using an analyzer (Thermo Scientific K-Alpha) with an aluminum anode (Al 1486.6 eV) as the X-ray source to verify the presence of sulfur vacancies. Raman measurements were performed on a Horiba LabRAM HR Evolution spectrometer at 532 nm excitation wavelength.

Electrochemical measurements

Electrochemical measurements were made by assembling a coin-cell (2032) in a glove box filled with argon gas and containing less than 0.1 ppm of oxygen and moisture. A pure lithium metal foil was used as the reference electrode. The electrolyte used was a 1 M LiPF$_6$ solution in diethyl carbonate/dimethyl carbonate/ethylene carbonate with a volume ratio 1/1/1. Where the amount of electrolyte was 30 μL on both sides of the separator, Celgard 2500 microporous membranes were used as separators. The Vs-CdS NWs@C electrode was prepared by mixing the active material, carbon black, and poly(vinylidene difluoride) (PVDF) in a mass ratio of 8:1:1. The mixed material was then uniformly dispersed in N-methylpyrrolidone (NMP) and magnetically stirred for 4 h to prepare the electrode slurry. It was then applied to the copper foil cleaned with anhydrous ethanol, and after drying, the copper foil was cut into 12-mm round electrode sheets. The mass of the active mass on the electrode sheet was calculated to be 0.8–1.5 mg cm^{-2}. Electrochemical impedance spectroscopy (EIS) and cyclic voltammetry (CV) tests were performed using a CHI760E electrochemical workstation (CHENHUA, Shanghai, China). Constant current charge/discharge (GCD), cycle stability, and rate performance measurements were performed using the NEWARE battery test system.

Results and discussion

Figure 1 shows the preparation process of Vs-CdS NWs@C composites. It was prepared by a PVP-assisted solvothermal method. First, the protonation reaction of ethylenediamine

Fig. 1 Schematic diagram of the synthesis process of Vs-CdS NWs@C

Vs-CdS NWs

Vs-CdS NWs@C

● Cd(CH$_3$COO)$_2$·2H$_2$O
● CH$_4$N$_2$S
• PVP
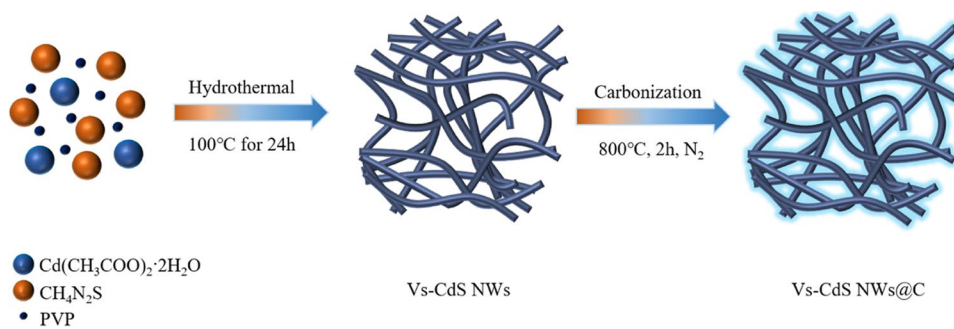
with water at 100 °C results in the formation of positively charged ammonium ions. Then the protonated ethylenediamine molecules are combined with S ligands to form adjacent CdS layers [38]. Meanwhile, excess thiourea can adsorb on the surface of primary nanocrystals, partially blocking the directional growth of the crystals, and a large number of sulfur vacancies were generated at low temperatures [39]. Finally, Vs-CdS NWs@C were constructed by 2-h high-temperature carbonization in N$_2$ atmosphere.

The material components of CdS and VS-CdS NWs@C were analyzed by XRD. The XRD patterns of CdS and VS-CdS NWs@C are shown in Fig. 2a. The sample has all strong diffraction peaks that are in accordance with the standard card of CdS (JCPDS No. 41–1049). Samples were free of obvious contaminants. The results show that this simple and low-cost PVP-assisted solvothermal method can obtain high-purity Vs-CdS NWs@C. The constituent

elements and valence states of the material were analyzed via XPS pattern. Figure 2b shows the XPS full spectrum of the Vs-CdS NWs@C material, and the XPS full spectrum of CdS can be seen in Fig. S1. All peaks in the XPS spectra have been corrected by a carbon peak at 284.8 eV. The presence of sulfur vacancies in Vs-CdS NWs@C can be observed in Fig. 2c, where the binding energy of the S 2p peak decreases from CdS (161.49 eV, 162.80 eV) to Vs-CdS NWs@C (160.37 eV, 161.68 eV), and the two characteristic peaks at 161.49 and 162.80 eV match the S 2p$_{3/2}$ and S 2p$_{1/2}$ orbitals, respectively. Report demonstrated that the S 2p$_{1/2}$ peak corresponding to low-coordination sulfur was related to sulfur vacancies[42]. Therefore, we have calculated a sulfur vacancy concentration (Vs) of 10.2% and the results are summarized in Table S2. Additionally, the Cd high-resolution profile has two distinct binding energy firm peaks at 405.01 and 411.76 eV (Fig. 2d) belonging to

Fig. 2 a XRD patterns of Vs-CdS NWs@C and CdS, **b** Vs-CdS NWs@C XPS full spectrum; XPS spectra of Vs-CdS NWs@C and CdS, **c** Cd 3d, and **d** S 2p
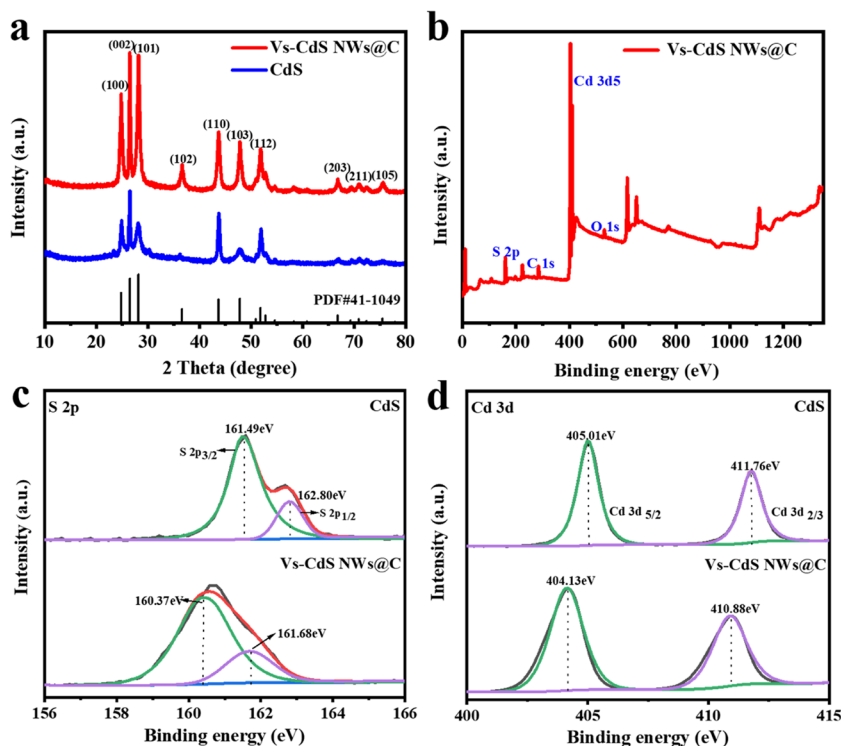
$Cd_{5/2}$ and $Cd_{3/2}$. At the same time, the Cd peaks (404.13 eV, 410.88 eV) of the Vs-CdS NWs@C are displaced to the lower binding energy region owing to the increase in the density of the Cd^{2+} electron cloud in the S vacancy region [40]. Figure S5 shows the Raman spectra of all samples at an excitation wavelength of 532 nm. The peaks at about 300 and 600 cm^{-1} are attributed to the first-order (1LO) and second-order (2LO) modes of CdS, respectively. In addition, from the VS-CdS NWs@C spectra, two peaks were clearly presented at 1350 and 1580 cm^{-1}, which can be attributed to the *D* and *G* bands of carbon, respectively. The $I_{D/G}$ ratio of the composite is about 1.01, indicating the amorphous carbon. This indicates that the material has been successfully carbon coated.

SEM and TEM are utilized to investigate the morphology and structure of the Vs-CdS NWs@C. A fluffy nanowire-like structure can be observed by SEM in Fig. 3(a, b). And the morphological structure of CdS can be seen in Fig. S2. As shown in Fig. 3c, the TEM images further indicate that the synthesized Vs-CdS NWs@C is in the form of fluffy

nanowires, which is consistent with the SEM results taken. This unique nanowire structure increases the specific surface area of the Vs-CdS NWs@C and increases the contact area between the Vs-CdS NWs@C electrode and the electrolyte. This structure also alleviates the volume expansion of the anode material during lithium-ion intercalation and deintercalation reactions. And the carbon coating improves the lack of electrical conductivity of the CdS. Meanwhile, the corresponding SAED map (Fig. 3e) shows the presence of multiple diffraction rings. The resulting Vs-CdS NWs@C is polycrystalline. Upon further analysis of Fig. 3d, the lattice plane spacing was measured to be 0.316 nm, which coincides with the (101) crystal plane of CdS [41]. In addition, the EDS elemental mappings are depicted in Fig. 3(g, f), illustrating the homogeneously dispersion of Cd, S, C, and N elements in the Vs-CdS NWs@C.

Figure 4a shows the CV curves of the Vs-CdS NWs@C electrode at a scanning rate of 0.1 mV s^{-1} in a voltage range of 0.05–3 V. It can be seen that there are two distinct cathode peaks in the discharge curve of the first
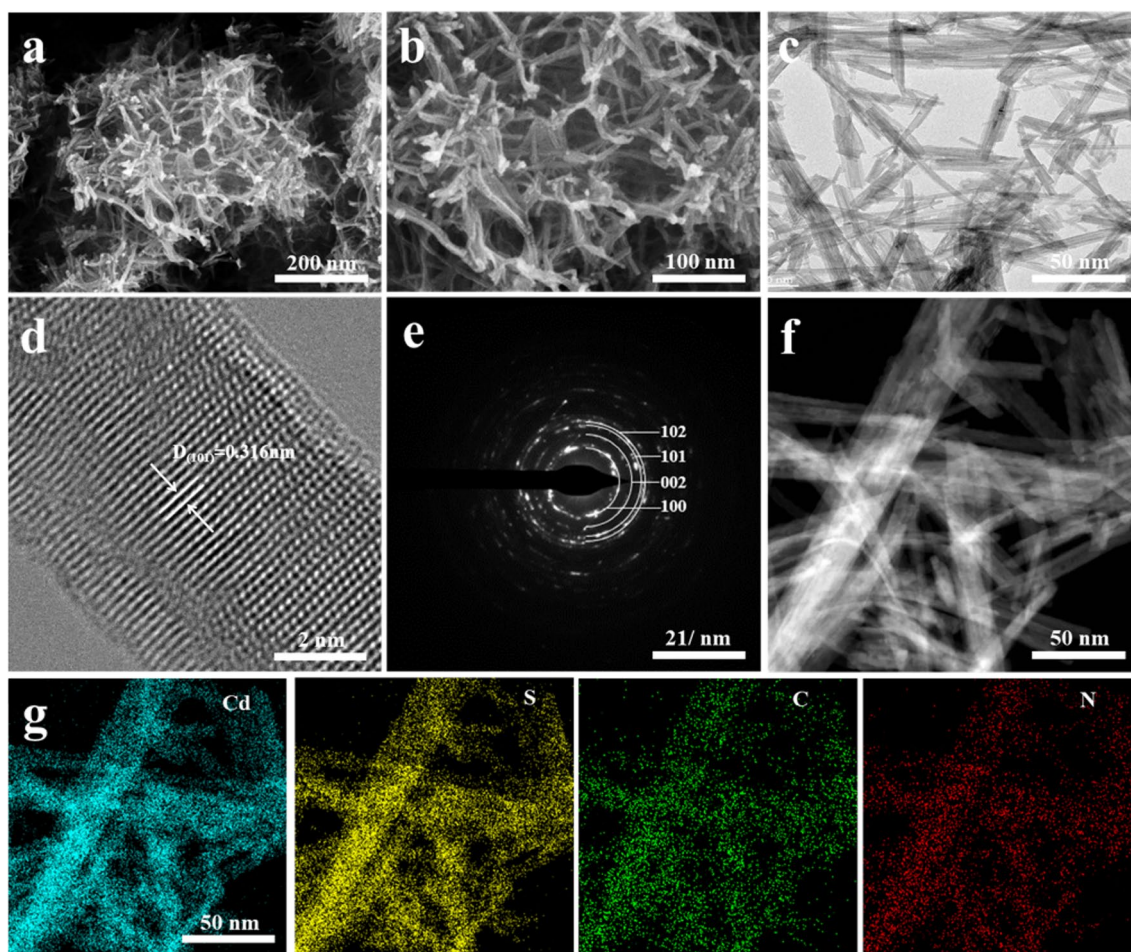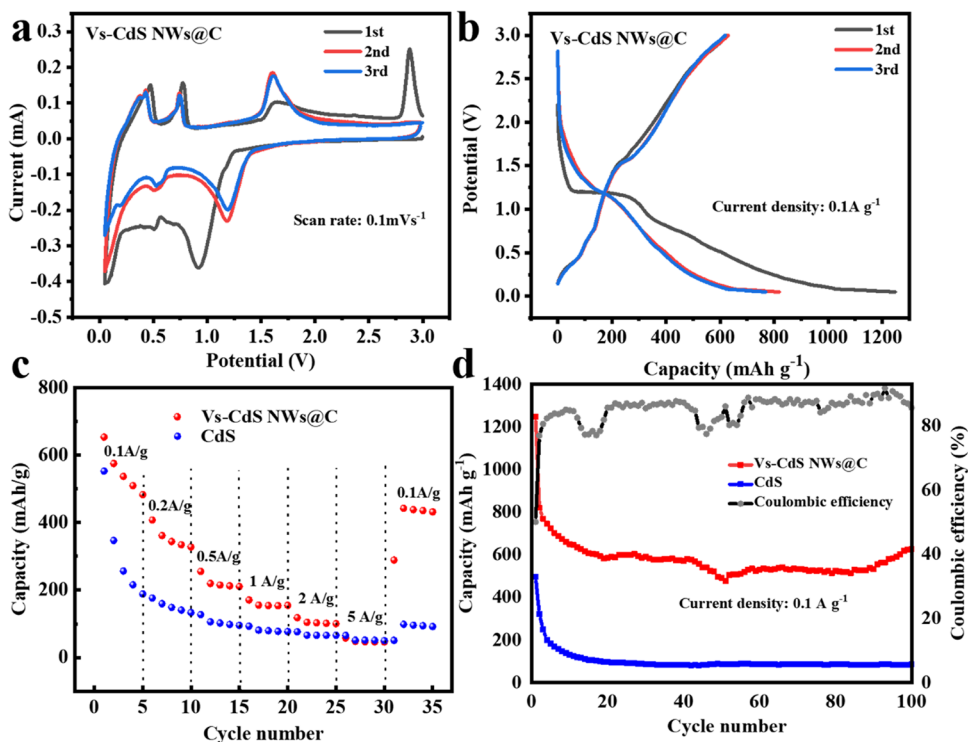

Fig. 3 Vs-CdS NWs@C: **a**, **b** SEM image, **c** TEM image, **d** HRTEM image, **e** SAED image, **f**, **g** HAADF-STEM image and EDS elemental mapping distribution of the Vs-CdS NWs@C

Fig. 4 **a** CV plot of the first three turns; **b** charge–discharge plot of the first three turns; **c** multiplier performance plot; **d** comparison of cycling performance comparison at 0.1 A g.$^{-1}$

cycle, corresponding to voltages of 0.93 V and 0.57 V, respectively. Meanwhile, the reaction processes correspond to the conversion of CdS to Cd and the alloying of Cd to Li$_3$Cd, respectively. In the charging curve of the first cycle, there are two distinct anodic peaks located at 0.7 V due to the dealloying reaction of Li$_3$Cd to Cd. The peak near 2.1 V is due to the reaction between the Cd and the Li$_2$S to form the CdS. Figure 4b depicts the typical GCD profiles of the Vs-CdS NWs@C electrode at a current density of 0.1 A g^{-1} between 0.05 and 3.0 V. A clear discharge plateau at 1.2 V and a clear charging plateau at 1.6 V appeared. It is noted that the plateau voltage in the GCD curves are consistent with the redox peak in the CV profiles. The discharging and charging capacities of the Vs-CdS NWs@C electrode were 1247.2 and 623.9 mAh g^{-1} in the first cycle, in which the second and third cycles basically coincide. For comparison, the GCD curves of the CdS electrode can be seen that the difference between the second and third cycles is large in Fig. S3. This fact can indicate that the Vs-CdS NWs@C electrode has higher specific capacity than CdS. As shown in Fig. 4c, the rate performances of CdS and Vs-CdS NWs@C electrode were measured at different current densities ranging from 0.1 to 5 A g^{-1}. The Vs-CdS NWs@C electrode shows the higher specific capacity, when the current density was set to 0.1, 0.2, 0.5, 1.0, 2.0, and 5.0 A g^{-1}, corresponding to the charge capacities of 536.8, 589.8, 361.5, 219.6, 155.3, 104.3, 263.8, and 46.7 mAh g^{-1}. When the current density is restored to 0.1

A g^{-1}, the specific capacity can still reach 442.56 mAh g^{-1}. The rate performance indicates that our structural design can facilitate electrolyte penetration and accelerate lithium ion transport at low current densities, allowing the conversion reaction to be completed thoroughly and high capacity to be achieved. However, at high current densities, kinetic polarization caused by ion transport resistance becomes severe, resulting in severe capacity degradation. Similarly, the cycling performance and capacity of Vs-CdS NWs@C electrode outperformed that of pure CdS electrodes in the cycling test (Fig. 4d). After 100 cycles, the Vs-CdS NWs@C electrode still maintains a capacity of 625.6 mAh g^{-1}. As the number of cycles increases, it can be seen that the Vs-CdS NWs@C electrode exhibits excellent stability at a current density of 0.2 A g^{-1} (Fig. S4). Excellent electrochemical performance of the Vs-CdS NWs@C electrode is attributed to the synergistic modulation strategy of its nanostructure, surface defect engineering, and carbon coating. They enhance the dispersion and conductivity of the material and also accelerate the ion/electron transport efficiency. In addition, we have carried out a comparison of the electrochemical performance, which can be seen in Table S1.

To further confirm the high reaction kinetics of Vs-CdS NWs@C electrode, CV curves from 0.2 to 1.0 mV s^{-1} were examined, as shown in Fig. 5a. Generally, the charge contributions contain two parts: redox pseudocapacitance and intercalation. The capacitive process shows high reaction kinetics. The degree of capacitive contribution can be
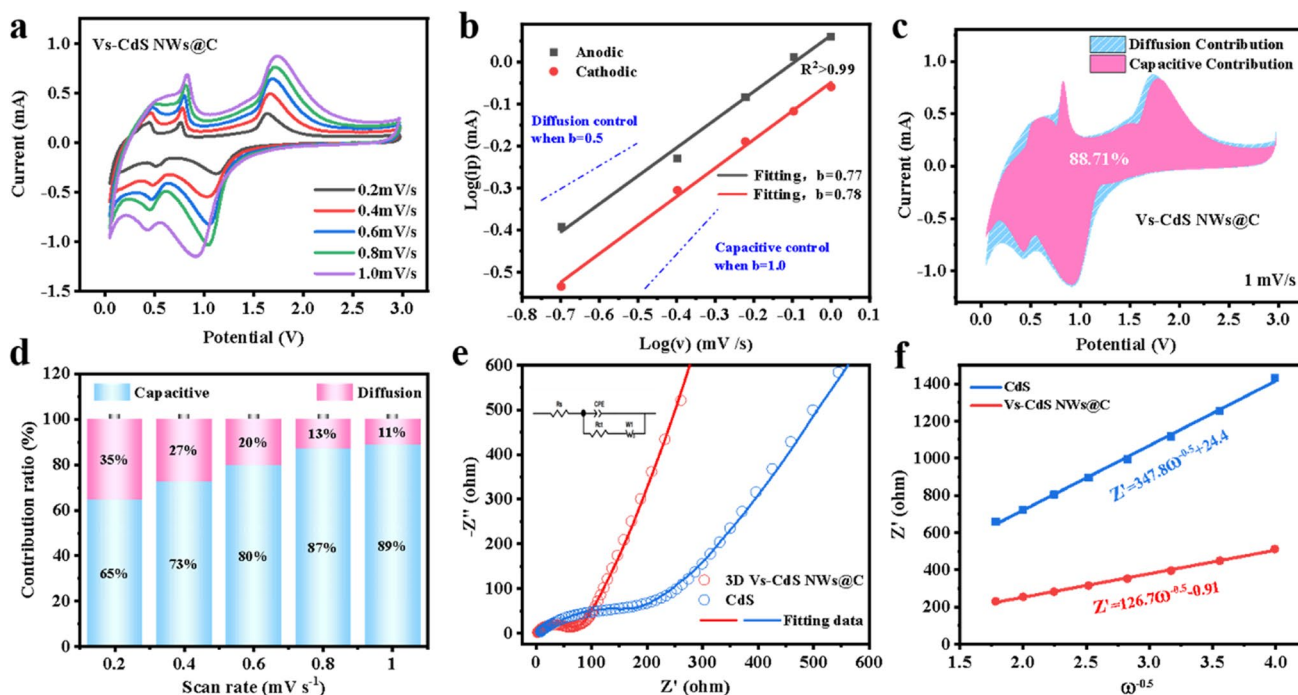
Fig. 5 a The CV profiles at different scan rates of the Vs-CdS NWs@C electrode; **b** *b*-value calculation results; **c** capacitive contribution to charge storage at a sweep speed of 1.0 mV s⁻¹; **d** contributions of the diffusion-controlled and capacitive capacity of the Vs-CdS NWs@C anode at diverse sweep speeds; **e** Nyquist plot; **f** relationship between the fundamental part of impedance and low frequencies

reflected by the *b*-value originated from the relationship between current (*i*) and scanning rate (*v*) in Eq. (1).

$$\mathrm{Log}\,i = b\,\mathrm{Log}\,v + \mathrm{Log}\,a \tag{1}$$

The *b*-values are between 0.5 and 1. If the *b*-value is close to 1, the capacitive contribution predominates. The *b*-values of Vs-CdS NWs@C electrode in the charging process are displayed in Fig. 5b. The *b*-values calculated according to Eq. (1) are 0.77 and 0.78, respectively, indicating a higher contribution of capacitance control and higher reaction kinetics.

In order to quantitatively analyze the capacitive and diffusive contributions, the current response (*i*) at potential (*V*) can be divided into two components as the capacitance-controlled contribution to the current ($k_1 v$) and the diffusion-controlled contribution to the current ($k_2 v^{1/2}$), as shown in Eq. (2).

$$\mathrm{I}(\mathrm{V}) = k_1 v + k_2 v^{1/2} \tag{2}$$

where $k_1 v$ at $b = 1$ and $k_2 v^{1/2}$ at $b = 0.5$ are associated with the capacitive and diffusion control processes, respectively. As shown in Fig. 5c, the CV curve at 1 mV s⁻¹ can be divided into two regions. The ratio of the two contributions is equal to the ratio of their areas. As shown in Fig. 5d, the capacitance contribution increases gradually with the increase of

scanning rate, and the capacitance contribution of Vs-CdS NWs@C electrode at 1.0 mV s⁻¹ is as high as 88.71%. It can be found that the capacitive part occupies the more considerable capacity contribution at high rates. This significantly enhanced pseudocapacitive effect of the Vs-CdS NWs@C electrode is responsible for its excellent reaction kinetics. It is attributed to its large surface area and sulfur vacancy, providing more active sites for surface reactions.

The Li⁺ diffusion kinetics and charge transfer behavior of the VS-CdS NWs@C and CdS electrodes were evaluated using the EIS experiments. Figure 5e depicts the Nyquist plots of the both electrodes after 100 cycles. An equivalent circuit model as shown in the inset of Fig. 5e was used to fit these spectra. In the EIS equivalent circuit, R_s in the high-frequency region is related to the bulk resistance of the battery; R_{ct} represents a charge transfer resistance; CPE are the corresponding capacitors for R_{ct}; W_1 is the Warburg impedance of Li⁺ migration in electrode materials. By fitting with the Zview program, the charge transfer resistance (R_{ct}) for the VS-CdS NWs@C and CdS electrodes was determined to be 54.6 and 147.1 Ω, respectively. The fitting parameters can be seen in Table S3. The charge transfer resistance of the Vs-CdS NWs@C electrode was significantly lower than that of the CdS electrode, indicating that the Vs-CdS NWs@C electrode has a faster surface electron mobility. In addition,

the diffusion coefficient of Li$^+$ ($D_{Li}{}^+$) can be calculated by following equation:

$$D_{Li^+} = \frac{R^2 T^2}{2A^2 n^4 F^4 C_{Li^+}^2 \sigma^2} \tag{3}$$

$$Z\prime = R_{ct} + R_s + \sigma \omega^{-0.5} \tag{4}$$

where R is the ideal gas constant, T is the absolute temperature, n is the number of electrons transferred per Li$^+$ during charging and discharging, F is Faraday's constant, $C_{Li}{}^+$ is the concentration of lithium ions contained per unit cell volume, A is the contact area of the electrode surfaces, σ is Warburg's diffusion constant, its value is obtained through Eq. (4), $Z\prime$ is the abscissa of the EIS spectrum, and $D_{Li}{}^+$ is the lithium-ion diffusion coefficient. The diffusion coefficient of the Vs-CdS NWs@C electrode was 2.92×10^{-16} cm^2 s^{-1} higher than that of the CdS (3.87×10^{-16} cm^2 s^{-1}) electrode. This is because that the large specific surface area and defect engineering can effectively shorten the Li$^+$ diffusion path and thus improve the Li$^+$ transport kinetics within the electrode.

Conclusion

In summary, we prepared Vs-CdS NWs@C by a PVP-assisted solvothermal method. The lithium-ion battery anode prepared by this method facilitates the diffusion of the electrolyte through the synergistic modulation of nanostructures, sulfur defects, and carbon coatings; improves the contact area of the Vs-CdS NWs@C electrode with the electrolyte; increases the structural stability; and alleviates the volume expansion of the Vs-CdS NWs@C electrode during lithium-ion intercalation/deintercalation. Therefore, when the Vs-CdS NWs@C electrode is used as the anode material, it shows remarkable cycling stability and excellent reversible capacity, which still gives a reversible capacity of 625.6 mAh g^{-1} after 100 cycles at a current density of 0.1 A g^{-1}. The nanowire structure and sulfur defects increase the electrode structure's active sites while enhancing the carbon coating's conductivity, resulting in superior electrochemical performance. Our results show that this idea provides a new avenue to design new LIB metal-sulfide anode materials with high specific surface area, sulfur-containing vacancies, and good electrical conductivity.

XPS full spectra, SEM image of CdS, Raman spectra of V$_S$-CdS NWs@C and CdS, and detailed electrochemical performance can be found in the supplementary information.

Author contribution Wenhua Tian: conceptualization, methodology, investigation, and writing—original draft. Peng Bai: resources and data curation. Guoqiang Ling: methodology and formal analysis. Zihan Wang: formal analysis and data curation. Jing Ren: conceptualization, validation, and writing—original draft. Rui-Peng Ren: conceptualization, writing—review and editing, supervision, and funding acquisition. Yong-Kang Lv: project administration and funding acquisition.

Data availability Data will be made available on request.

Declarations

Competing interests The authors declare no competing interests.

Ethical approval Not applicable.

Conflict of interest The authors declare no competing interest.

References

1. Wang R, Cui W, Chu F, Wu F (2020) Lithium metal anodes: present and future, Journal of Energy. Chemistry 48:145–159

2. Shi C, Alexander GV, O'Neill J, Duncan K, Godbey G, Wachsman ED (2023) All-solid-state garnet type sulfurized polyacrylonitrile/lithium-metal battery enabled by an Inorganic Lithium conductive salt and a bilayer electrolyte architecture. ACS Energy Lett 8:1803–1810

3. Li Z, Hu X, Shi Z, Lu J, Wang Z (2021) MOF-derived iron sulfide nanocomposite with sulfur-doped carbon shell as a promising anode material for high-performance lithium-ion batteries. J Alloy Compd 868:159110

4. Horwitz NE, Shevchenko EV, Park J, Lee E, Xie J, Chen B, Zhong Y, Filatov AS, Anderson JS (2020) Synthesis, modular composition, and electrochemical properties of lamellar iron sulfides. J Mater Chem A 8:15834–15844

5. Yu WJ, Liu C, Zhang L, Hou PX, Li F, Zhang B, Cheng HM (2016) Synthesis and electrochemical lithium storage behavior of carbon nanotubes filled with iron sulfide nanoparticles. Adv Sci 3:1600113

6. Xi Y, Ye X, Duan S, Li T, Zhang J, Jia L, Yang J, Wang J, Liu H, Xiao Q (2020) Iron vacancies and surface modulation of iron disulfide nanoflowers as a high power/energy density cathode for ultralong-life stable Li storage. J Mater Chem A 8:14769–14777

7. Ren J, Ren RP, Lv YK (2020) Hollow I-Cu$_2$MoS$_4$ nanocubes coupled with an ether-based electrolyte for highly reversible lithium storage. J Colloid Interf Sci 577:86–91

8. Zhou N, Qin W, Wu C, Jia C (2020) Graphene-attached vanadium sulfide composite prepared via microwave-assisted hydrothermal method for high performance lithium-ion batteries. J Alloy Compd 834:155073

9. Zhao J, Xiao D, Wan Q, Wei X, Tao G, Liu Y, Xiang Y, Davey K, Liu Z, Guo Z, Song Y (2023) Molybdenum atom engineered vanadium disulfide for boosted high-capacity Li-ion storage. Small 19:2301738

10. Li L, Li Z, Yoshimura A, Sun C, Wang T, Chen Y, Chen Z, Littlejohn A, Xiang Y, Hundekar P, Bartolucci SF, Shi J, Shi S-F, Meunier V, Wang G-C, Koratkar N (2019) Vanadium disulfide flakes with nanolayered titanium disulfide coating as cathode materials in lithium-ion batteries. Nat Commun 10:1764

11. Cao X, Min W, Chen P, Xu D, Liu D, Wang R (2022) Controllable synthesis of hierarchical core-shell NiS_2/CoS_2@N, S-C nanospheres for lithium storage. J Alloy Compd 911:165112

12. Santhosh NM, Shaji N, Stražar P, Filipič G, Zavašnik J, Ho CW, Nanthagopal M, Lee CW, Cvelbar U (2022) Advancing Li-ion storage performance with hybrid vertical carbon/Ni_3S_2-based electrodes. J Energy Chem 67:8–18

13. Tronganh N, Gao Y, Jiang W, Tao H, Wang S, Zhao B, Jiang Y, Chen Z, Jiao Z (2018) Hierarchically assembled 3D nanoflowers and 0D nanoparticles of nickel sulfides on reduced graphene oxide with excellent lithium storage performances. Appl Surf Sci 439:386–393

14. Peng W, Zhang J, Li S, Liang J, Hu R, Yuan B, Chen G (2022) Rationally integrated nickel sulfides for lithium storage: S/N co-doped carbon encapsulated NiS/Cu_2S with greatly enhanced kinetic property and structural stability. Inorg Chem Front 9:2023–2035

15. Zong J, Wang F, Liu G, Zhao M, Yang S, Song X (2019) Ethylene glycol solvent induced expansion of interplanar spacing and 2H–1T phase transformation of molybdenum disulfide nanocomposites for enhanced lithium storage capability. J Alloy Compd 810:151959

16. Chen M, Wang J, Yan X, Ren J, Dai Y, Wang Q, Wang Y, Cheng X (2017) Flower-like molybdenum disulfide nanosheets grown on carbon nanosheets to form nanocomposites: novel structure and excellent electrochemical performance. J Alloy Compd 722:250–258

17. Kotsun AA, Alekseev VA, Stolyarova SG, Makarova AA, Grebenkina MA, Zubareva AP, Okotrub AV, Bulusheva LG (2023) Effect of molybdenum disulfide doping with substitutional nitrogen and sulfur vacancies on lithium intercalation. J Alloy Compd 947:169689

18. Wu T, Jing M, Liu Y, Ji X (2019) Binding low crystalline MoS_2 nanoflakes on nitrogen-doped carbon nanotube: towards high-rate lithium and sodium storage. J Mater Chem A 7:6439–6449

19. Qin S, Lei W, Liu D, Chen Y (2016) Advanced N-doped mesoporous molybdenum disulfide nanosheets and the enhanced lithium-ion storage performance. J Mater Chem A 4:1440–1445

20. Tang Z-R, Han B, Han C, Xu Y-J (2017) One dimensional CdS based materials for artificial photoredox reactions. J Mater Chem A 5:2387–2410

21. Kumar SG, Rao KSRK (2014) Physics and chemistry of CdTe/CdS thin film heterojunction photovoltaic devices: fundamental and critical aspects. Energy Environ Sci 7:45–102

22. Kim H-I, Kwon OS, Kim S, Choi W, Kim J-H (2016) Harnessing low energy photons (635 nm) for the production of H_2O_2 using upconversion nanohybrid photocatalysts. Energy Environ Sci 9:1063–1073

23. Xu P, Liu J, Yan P, Miao C, Ye K, Cheng K, Yin J, Cao D, Li K, Wang G (2016) Preparation of porous cadmium sulphide on nickel foam: a novel electrode material with excellent supercapacitor performance. J Mater Chem A 4:4920–4928

24. Patil SB, Kishore B, Vishwanatha R, Ebeling G, Nagaraju G (2019) CdS@MoS_2 core-shell nanospheres: a new electrode for lithium-ion batteries. J Mater Sci-Mater El 30:14456–14463

25. Zeng M, Chai Z, Deng X, Li Q, Feng S, Wang J, Xu D (2016) Core-shell CdS@ZIF-8 structures for improved selectivity in photocatalytic H_2 generation from formic acid. Nano Res 9:2729–2734

26. Li Y, Niu D, Fu X, Zhang Z, Zhang X (2021) A facile electrochemical strategy for engineering sulfur deficiencies of CdS nanosheets to promote the catalytic conversion of polysulfides for lithium–sulfur batteries, Sustain. Energy Fuels 5:678–686

27. Tian Q, Chen Y, Zhang W, Sui Z, Yang L (2020) Reducing the excessive interior space of SnO_2@C nanotubes by encapsulating SnO_2 nanowires for high lithium storage. J Alloy Compd 820:153404

28. Yang M, Yuan F, Shi W, Ren W, Guo M, Ouyang C, Zhou L, Sun N, Xiao Y, Xu E, Zhang X, Wei Y, Deng X, Nan C, Wang X, Shen Y (2023) Sub-nanowires boost superior capacitive energy storage performance of polymer composites at high temperatures. Adv Funct Mater 33:2214100

29. Storan D, Ahad SA, Forde R, Kilian S, Adegoke TE, Kennedy T, Geaney H, Ryan KM (2022) Silicon nanowire growth on carbon cloth for flexible Li-ion battery anodes. Mater Today Energy 27:101030

30. Wei H, Ma J, Li B, An L, Kong J, Yu P, Xia D (2016) Tuning ultrafine manganese oxide nanowire synthesis seeded by Si particles and its superior Li storage behaviors. NPG Asia Mater 8:e255–e255

31. Yu L-Q, Zhao S-X, Yuan Y, Wei G-D, Zhao J-W (2021) Mo-doped induced amorphous phase and sulfur vacancy healing in VS_4 for enhancing the storage of lithium ions. J Mater Chem A 9:1100–1109

32. Yan Z, Sun Z, Zhao L, Liu H, Guo Z, Qiu Y, Wang P, Qian L (2022) In-situ induced sulfur vacancy from phosphorus doping in FeS_2 microflowers for high-efficiency lithium storage. Mater Today Nano 20:100261

33. Huang Y, Ding S, Xu S, Ma Z-F, Yuan X (2022) Binder-free SnS_2 sheet array with high sulfur vacancy concentration for enhanced lithium storage performance. Electrochim Acta 409:139979

34. Liu G, Zhang T, Li X, Li J, Wu N, Cao A, Yuan W, Pan K, Guo D, Liu X (2023) MoS_2@C with S vacancies vertically anchored on V_2C-MXene for efficient lithium and sodium storage. Inorg Chem Front 10:1587–1602

35. Zhang X, Ou-Yang W, Zhu G, Lu T, Pan L (2019) Shuttle-like carbon-coated FeP derived from metal-organic frameworks for lithium-ion batteries with superior rate capability and long-life cycling performance. Carbon 143:116–124

36. Li H, Lu C-X (2015) Preparation and lithium storage performance of a carbon-coated Si/graphene nanocomposite. Carbon 81:850–852

37. Yin H, Jia L, Li HY, Liu A, Li G, Zhu Y, Huang J, Cao M, Hou Z (2023) Point-cavity-like carbon layer coated SnS nanotubes with improved energy storage capacity for lithium/sodium ion batteries. J Energy Storage 65:107354

38. Lv J, Liu J, Zhang J, Dai K, Liang C, Wang Z, Zhu G (2018) Construction of organic–inorganic cadmium sulfide/diethylenetriamine hybrids for efficient photocatalytic hydrogen production. J Colloid Interf Sci 512:77–85

39. Zhang J, Wang Y, Cui J, Wu J, Li Y, Zhu T, Kang H, Yang J, Sun J, Qin Y, Zhang Y, Ajayan PM, Wu Y (2019) Water-soluble defect-rich MoS_2 ultrathin nanosheets for enhanced hydrogen evolution. J Phys Chem Lett 10:3282–3289

40. Jiang C, Xu X, Mei M, Shi F-N (2017) Coordination polymer derived sulfur vacancies rich CdS composite photocatalyst with nitrogen doped carbon as matrix for H_2 production. ACS Sustainable Chem Eng 6:854–861

41. Cheng L, Li Y, Chen A, Zhu Y, Li C (2020) Impacts on carbon dioxide electroreduction of cadmium sulfides via continuous surface sulfur vacancy engineering. Chem Commun 56:563–566

42. Wang W, Li J, Jin Q, Liu Y, Zhang Y, Zhao Y, Wang X, Nurpeissova A, Bakenov Z (2021) Rational construction of sulfur-deficient $NiCo_2S_4$–x hollow microspheres as an effective polysulfide immobilizer toward high-performance lithium/sulfur batteries. ACS Applied Energy Materials 4:1687–1695